CrossMark

Structural and impedance spectroscopic analysis of Sr/Mn modified BiFeO$_3$ multiferroics

Muhammad Amin[1] · Hafiz Muhammad Rafique[1] · Muhammad Yousaf[1] · Shahid Mahmood Ramay[2] · Shahid Atiq[3]

Abstract Glycine + urea are used as fuel agents to synthesize polycrystalline nano-particles of as-burnt Bi$_{0.9}$Sr$_{0.1}$FeO$_3$ and Bi$_{0.9}$Sr$_{0.1}$Fe$_{1-x}$Mn$_x$O$_3$ (x = 0, 0.05, 0.10, 0.15 and 0.20) multiferroic samples using sol–gel auto-combustion method, at relatively low temperature. Structural analysis exhibits the formation of phase pure nano-composites having rhombohedral distorted perovskite structure belonging to space group R3c. Doping of Sr and Mn didn't disturb the crystal symmetry of the original composite. Field emission scanning electron microscopy revealed that the grains which were initially interlinked with each other became relatively isolated, uniformly distributed and spherical shaped with increasing Mn contents along with increased intergranular porosity. Energy dispersive X-ray spectroscopy confirms the at.% and wt% of all the elements, corresponding to each stoichiometric formula. Dielectric parameters for each sample depict conventional ferrite behavior while hopping of oxygen vacancies contributes a lot in conductivity of the samples. Contribution of grains, grain boundaries and interfaces are evident from impedance spectroscopy. Non-Debye type relaxation is confirmed from the frequency dependent electric modulus and Cole–Cole plots. A solid correlation has been established between electrical properties and microstructure of the samples under investigation.

1 Introduction

Multiferroics (MFs) are the materials which display more than one ferroic characteristics in the same phase [1]. MFs constitute an energetic group of materials which exhibit numerous properties and phenomena that are beneficial for manufacturing of a wide range of multifunctional devices. These materials have a prodigious research interest due to both, rich fundamental physics and a number of promising applications in modern technologies ranging from giant electric transformers to small computer memory devices or even tiny sensors [2]. The materials that exhibit magnetization and polarization simultaneously are called magneto-electric (ME) MFs. The ME coupling is the key feature of ME devices [3]. Our requirement is a material with a large ME effect at room temperature (RT). Among existing MFs, bismuth ferrite, BiFeO$_3$ (BFO) is a unique MF composite that fulfills the basic requirements of ME-MFs at RT. It has a ferroelectric Curie temperature of $\sim$1103 K and anti-ferromagnetic Neel temperature of $\sim$643 K [4]. At ambient conditions, it has rhombohedral distorted perovskite structure belonging to space group R3c (161). The rhombohedral lattice parameters of BFO are $a_{rh} = 3.96$ Å, while in hexagonal structure, they are $a_{hex} = b_{hex} = 5.58$ Å and $c_{hex} = 13.90$ Å [5]. Practical applications of BFO are hindered due to some major drawbacks such as weak magnetization owing to canted antiferromagnetic order, weak ME coupling and high leakage current density [6]. Most of these problems are the result of structural imperfections such as oxygen vacancies, pores, valence fluctuations of Fe ions and secondary phases [7, 8]. The main issue with BFO is its

✉ Muhammad Amin
saggar262@gmail.com

1 School of Physical Sciences, University of the Punjab, Lahore 54590, Pakistan

2 Department of Physics and Astronomy, College of Science, King Saud University, P. O. Box 2455, Riyadh 11421, Saudi Arabia

3 Centre of Excellence in Solid State Physics, University of the Punjab, Lahore 54590, Pakistan

conducting grain boundaries and domain walls at RT leading to a large loss factor that produces heating of a device which may destroy it. If tackled successfully, BFO might find potential applications in microwave technology, spintronic devices, sensors, recording and storage media, micro-actuators, nonvolatile logic and memory devices [9, 10]. However, in order to materialize BFO based multifunctional devices, it is necessary to improve its MF properties by minimizing the problems associated with it. Usually, chemical composition, synthesis procedures, chemistry, processing atmosphere, sintering temperature and substituted ions dictate the properties of BFO MFs. A lot of research is going on to produce suitably doped BFO materials using various techniques in order to achieve the required results. For example, larger dielectric constant, smaller dielectric loss, increased resistivity and decreased leakage current were observed in Mn-doped BFO [11, 12]. Decreased leakage current was also observed when pure BFO was co-doped with In and Mn [7]. In addition, when Sr was doped at Bi site in BFO, it reduced the oxygen vacancies which led to the reduction of dielectric loss, and hence overcoming the problem of leakage current [13]. The lowest leakage current in Nd/Mn-doped BFO thin films was achieved by Kawae [14]. Keeping in view the literature survey, we have been motivated for the co-doping of Sr^{2+} at Bi^{3+} site and Mn^{4+} at Fe^{3+} site in BFO to investigate the combined effect of these dopants especially on its dielectric properties. Sr^{2+} helps in suppressing the secondary phases [15] and decreasing the dielectric loss [13] whereas Mn^{4+} reduces the fluctuation of the Fe valencies which in turn diminishes the oxygen vacancies; an important factor to decrease leakage current in BFO system [16]. In this work, Sr/Mn-doped BFO nanoparticles (NPs) are prepared using sol–gel auto-combustion method. It is a distinctive technique to produce phase pure oxide materials having advantages of less energy consumption, cost saving instrumentation and self-purification due to highly exothermic reactions involved.

2 Experimental details

As-burnt $Bi_{0.9}Sr_{0.1}FeO_3$ (residue-BSFO-S1) and $Bi_{0.9}Sr_{0.1}Fe_{1-x}Mn_xO_3$ (BSFMO) (x = 0, 0.05, 0.10, 0.15 and 0.20 symbolized as S2, S3, S4, S5 and S6, respectively) are synthesized by sol–gel auto-combustion method at relatively low temperature. Bismuth nitrate [$Bi(NO_3)_2 \cdot 5H_2O$, Sigma Aldrich, 99.9 %], strontium nitrate [$Sr(NO_3)_2$, Merck, 99.9 %], iron nitrate [$Fe(NO_3)_3 \cdot 9H_2O$, Merck, 99.9 %] and manganese nitrate [$Mn(NO_3)_2$, 99.9 %, Merck] were used as raw materials. $Bi(NO_3)_2 \cdot 5H_2O$, being less soluble in deionized water, was dissolved separately in 3 M HNO_3 with continuous stirring by magnetic capsule to make a transparent solution. The other nitrates were

dissolved in deionized water. After mixing the two solutions, the stoichiometric amounts of urea and glycine were added. The precursor was put on a hot plate at 85 °C with continuous stirring until it converted into a dark viscous resin. When gel was formed, the temperature was raised up to 350 °C. This continuous increase in temperature led to auto-ignition with the release of gases as a result of exothermic reaction. The resultant powder samples were calcined at 550 °C for 3 h using a muffle furnace. A steel dye of 10 mm diameter was used to make pellets from powder by applying a pressure of 4 tons using an Apex hydraulic press. A Rigaku D/MAX-IIA X-Ray diffractometer (XRD) with CuK_α radiation, a NovaNano SEM 450-field emission scanning electron microscope (FESEM) along with energy dispersive X-ray spectroscopy (EDX) and a precision impedance analyzer, 6500B through a wide range of frequency (20 Hz–20 MHz) were used to investigate the structural, morphological, compositional and dielectric characteristics of the prepared samples, respectively. All characterizations are performed at RT.

3 Results and discussion

Figure 1 shows the XRD patterns obtained for residue-BSFO (S1) and BSFMO (S2–S6) samples. The pattern S1 reveals an amorphous phase, as several broad diffraction peaks can be seen in it. The crystallinity is obtained rapidly when residue-BSFO is calcined at 550 °C for 3 h, as shown by pattern S2. It can be inferred that no crystallinity develops in BFO ceramics without calcination. It is concluded that calcination temperature is the most important parameter for developing crystalline phase during synthesis
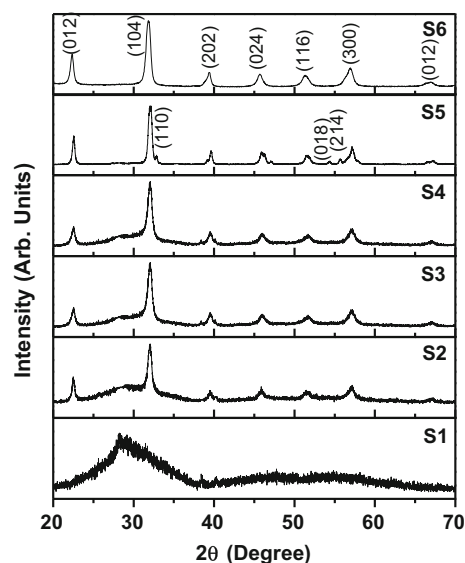

Fig. 1 XRD patterns of all the samples

of BFO. The phase diagram of Fe_2O_3 and Bi_2O_3 showing BFO with undesired impurities also confirms the importance of controlling the calcination temperature for synthesizing single crystal BFO [5]. All the major peaks of all other XRD patterns of samples matched well with ICSD reference no. 01-071-2494. This confirms the formation of phase pure rhombohedral distorted perovskite structure having space group R3c (161) related to BFO. This means that doping of Sr and Mn in BFO does not alter its crystal symmetry. It has also been proved already that the substitution of Mn and Sr in BFO do not disturb the lattice symmetry of BFO [13]. The absence of impurity peaks in all the patterns may be the result of Sr doping in BFO because it has been proved that doping of Sr^{2+} with limited contents hinders the formation of impurity phases in BFO-based MFs, without affecting the crystal structure [15]. Intensities of all the peaks increase slightly with Mn contents. As the peak intensity is linked to the amplitude of rotation of the octahedra [17], therefore the amplitude of tilt of rhombohedral distortion increases. The most intense diffraction peaks in each pattern were considered in order to calculate the crystallite size using Scherrer's equation [18], given as:

$$D = k\lambda / \beta \cos \theta \tag{1}$$

where D = crystallite size, k = 0.89, called sample shaped factor, λ is the wavelength of radiation used (1.5406 Å), β is the full width at half maximum in radians and θ is Bragg's angle in degrees. A slight difference is observed among the widths of the peaks of the doped composites and hence, the differences among crystallite sizes are smaller (9–15 nm). It is anticipated that impurity free BFO nanostructures will help to improve its MF properties. No shifting of any peak is observed towards higher or smaller angles after Sr and Mn doping in BFO. This may be due to the difference in ionic radius of Sr^{2+} (1.18 Å) which is larger than Bi^{3+} (1.03 Å), and Mn^{4+} (0.53 Å) which is smaller than Fe^{3+} (0.645 Å). These differences in radii of the dopants and hosts compensate the contraction or expansion of unit cell, resulting in almost no distortion of the crystal structure. This also confirms the 100 % incorporation of dopant ions at the host sites. The evaluated structural parameters are provided in Table 1. The c/a ratio of the unit cells of all the samples remains almost constant throughout the series which confirms a little change in all the cell parameters. Bulk BFO phase is generally formed at temperatures above 825 °C when synthesized via conventional solid state reaction process [19]. The present study confirms that a heat treatment at 550 °C for 3 h is required to transform the gel into oxide in case of BFO, which has been reported earlier, as well [20]. It can be inferred that synthesis of pure BFO MFs at lower temperatures can prevent the vaporization of Bi^{3+} due to its volatile nature at high temperature resulting in secondary phases along with BFO limiting its use in multifunctional devices.

FESEM micrographs shown in Fig. 2a–d elucidate the grains growth, voids, boundaries and surface morphology of the samples under investigation. The images shown in Fig. 2a, b, relating to samples S2 and S3 reveal that most of the grains are agglomerated as sharp edges are not clearly seen. As the Mn contents are increased in the series, some better separated grains with fine edges and a homogenous morphology are observed (Fig. 2c). With further increase in Mn contents, as displayed by image Fig. 2d, the grains retained their spherical shapes and homogeneity, while the porosity was increased slightly. Further, it depicted well shaped, uniformly distributed and spherical-shaped grains. This gradual refinement of the structural morphology might have improved the crystallinity of the samples, well consistent with the diffraction data, as the diffraction pattern of S6 showed the most intense diffraction peaks, corresponding to the highest crystallinity in the series of samples. Average grain sizes, evaluated from SEM images, are in the range of 50–80 nm. Some large sized grains could be the result of agglomeration of small sized grains. EDX spectra of $Bi_{0.9}Sr_{0.1}FeO_3$ and $Bi_{0.9}Sr_{0.1}Fe_{0.80}Mn_{0.2}O_3$, shown in Fig. 2e, f confirm the stoichiometric at.% and wt% of all the elements present in the samples. No impurity peaks are seen in the spectra confirming the validity of the sol–gel based combustion technique to prepare the phase-pure samples. Quantitative data set of EDX analysis of BSFO and BSFMO samples is provided in Table 2.

Real (ε') and imaginary (ε'') parts of dielectric constant (ε) are displayed in Fig. 3a, b. It can be seen that intense dielectric dispersion exists with increasing frequency in ε' and ε'' for BSFMO samples (except S6). Both ε' and ε'' decrease with increasing frequency. According to Kumar [21], polarization lags behind the applied field due to inertia. In the low frequency region, atomic, electronic, interfacial and ionic polarizations contribute, resulting in high value of ε. At a certain increased frequency, the only contribution to the polarization comes from electric polarization, others being locked due to having larger relaxation times and hence, the ε is decreased. Similar trend related to ε has been reported in Mn [22] and Sr [23] doped BFO ceramics. These types of processes can be discussed on the basis of Maxwell–Wagner model [24] and Koop's theory [25]. At lower frequency, ε increases with increased Mn contents and has maximum value for 15 % Mn doping. For 20 % Mn-doped sample, the unit cell volume decreases due to the smaller ionic radius of Mn compared to Bi. In the oxygen octahedral (FeO_6), the free space for the movement of Fe^{3+} ions becomes lesser and hence, polarization decreases which reduces ε.

Dissipation of energy in dielectrics is called dielectric loss (tan δ). It is reported that impurities, defects and

Table 1 Calculated parameters of the doped BFO samples

Composition	Crystallite size (nm)	a (Å)	c (Å)	c/a	Volume (Å^3)
BiFeO$_3$		5.5876	13.8670	2.4817	374.94
ICSD reference code = 01-071-2494					$\sim$375
Sr$_{0.1}$Bi$_{0.9}$FeO$_3$	9.2	5.61	13.92	2.4813	379
Sr$_{0.1}$Bi$_{0.9}$Fe$_{0.95}$Mn$_{0.05}$O$_3$	10.3	5.59	13.89	2.4848	376
Sr$_{0.1}$Bi$_{0.9}$Fe$_{0.90}$Mn$_{0.10}$O$_3$	13.5	5.58	13.88	2.4874	374
Sr$_{0.1}$Bi$_{0.9}$Fe$_{0.85}$Mn$_{0.15}$O$_3$	13.8	5.56	13.85	2.4910	371
Sr$_{0.1}$Bi$_{0.9}$Fe$_{0.80}$Mn$_{0.20}$O$_3$	15	5.54	13.83	2.4964	368

Fig. 2 FESEM images of **a** S2, **b** S3, **c** S4, **d** S6 and EDX spectra of **e** S2 and **f** S6 samples
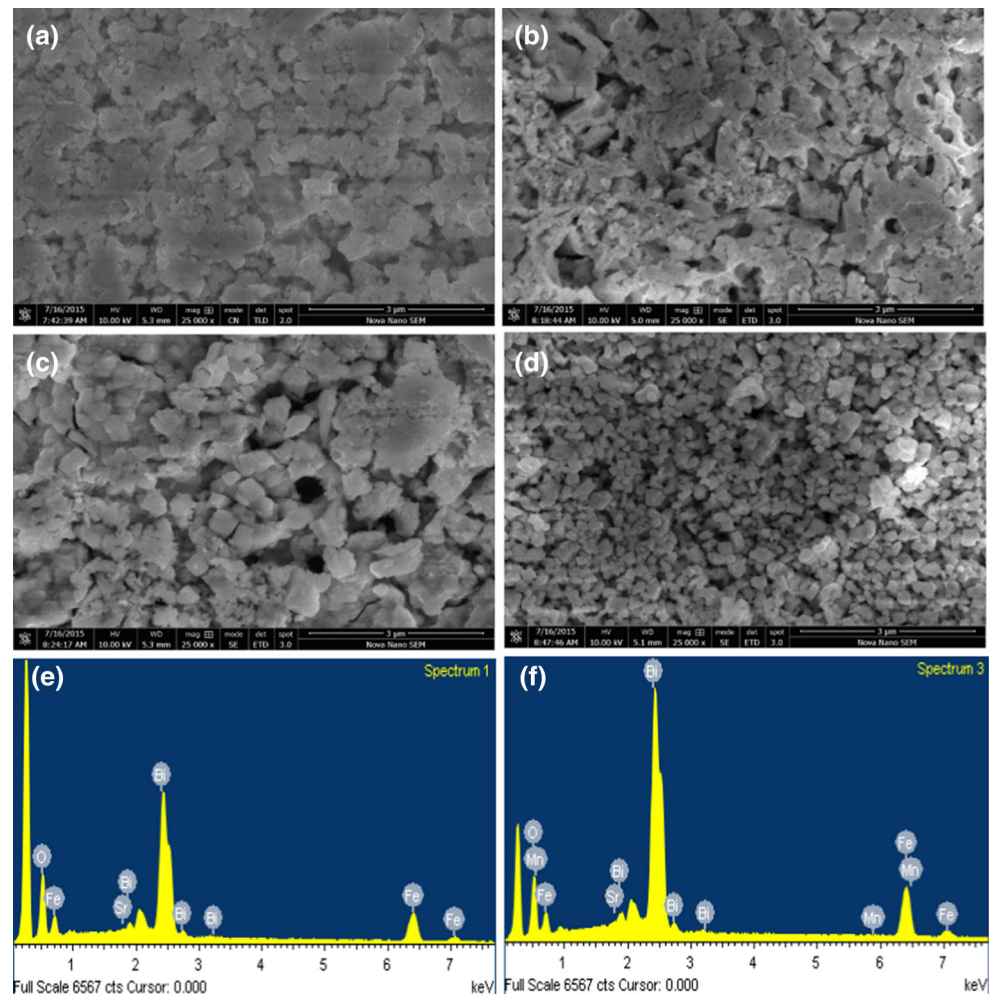
imperfections in the crystal lattice are responsible for dielectric losses in materials which cause polarization to lag behind with the applied external field [26]. Further, it has been reported by Wei et al. [13] that oxygen vacancies are one of the main causes for the high leakage current density in BFO. It is also believed that high leakage current causes the high dielectric loss in BFO [27]. Oxygen vacancies are also a form of impurities and defects so it can be concluded that the impurities and defects cause dielectric losses. It is evident from Fig. 3c, that the dielectric loss

of all the doped samples decreases up to a wide frequency range as the doping concentration increases. This reduction in dielectric loss recommends that co-doping of Sr and Mn in BFO ceramics causes the reduction of oxygen vacancies (V$_o$). These vacancies might have created during heat treatment at high temperature because of relatively highly volatile nature of Bi due to its low melting and boiling points. Presence of V$_o$ cause the valence states of iron (Fe^{3+}–Fe^{2+}) to fluctuate due to electron exchange which contributes significantly in conductivity of the materials. It

Table 2 Quantitative data of BSFO and BSFMO samples

Elements	BSFO		BSFMO	
	wt%	at.%	wt%	at.%
Bi	61.96	16.37	66.64	22.14
Sr	0.29	0.18	0.56	0.45
Fe	19.01	18.79	20.93	26.02
Mn	–	–	0.04	0.05
O	18.74	64.66	11.83	51.34
Total	100.00		100.00	

is concluded that Sr/Mn co-doping decreases the leakage problems of BFO ceramics which consequently reduces the dielectric loss. The observed Debye peaks or relaxation phenomenon in S3, S4 and S5 samples (Fig. 3c) may be the result of ferromagnetic resonance where frequency of applied field and electron hopping frequency coincides [28]. At higher frequencies, BSFMO NPs exhibit dielectric constant larger than 200 while dielectric loss less than 1 which suggests that the present compositions can be used to design microwave/high frequency devices.

Study of electrical conductivity is usually adopted to explore the relation between macroscopic measurement and microscopic movement of ions in ionic oxides. We can calculate *ac* conductivity (σ_{ac}) using the following formula:

$$\sigma_{ac} = \varepsilon' \varepsilon_o \omega \tan \delta \tag{2}$$

where ε_o is vacuum permittivity and ω is angular frequency. Frequency dependent σ_{ac} spectra of BSFMO ceramics is shown in Fig. 4a. The plots display a low frequency plateau and high frequency dispersions. According to Koop's model [25], in heterogeneous structures, poor conducting grain boundaries and highly conducting grains are responsible for low and high conductivity in lower and higher frequency regions,

respectively. The behavior of conductivity recommends that σ_{ac} obeys Jonsher's power law [29]:

$$\sigma_{ac}(\omega) = \sigma(0) + A\omega^n \tag{3}$$

here, first term is the frequency independent part (*dc* or electronic) of σ_{ac}, A is an amplitude constant that controls the polarization, *n* ($0 < n < 1$) is the index whose value depends upon the temperature and doping concentrations, hence it shows the collaboration of mobile ions with the lattice. At lower frequencies, σ_{ac} remains almost frequency independent while at higher frequencies, σ_{ac} is directly related with ω^n. Value of *n* varies between 0.62 and 0.85 with Mn contents, as shown in Fig. 4b, which indicates that hopping conduction phenomena exists in the present compositions.

Complex impedance spectroscopy (CIS) is employed to examine the conduction mechanism in different phases (microstructures) within polycrystalline and ionic materials. Here, an *ac* signal is applied through a sample in pellet form and output response is noticed [30]. A decrease in real (Z′) and imaginary (Z″) parts of impedance, as evident from Fig. 5a, b, is the result of enhanced conduction due to hopping of electrons between the localized ions which increases with frequency of electric field [31]. In high frequency region, both Z′ and Z″ become independent of frequency. Similar type of behavior is also reported by Singh et al. [32] for some other materials. The value of Z′ reduces as a function of Mn contents in BFO up to 15 %, which demonstrates the increased conductivity within the samples. According to heterogeneous two-layered model, polycrystalline materials are composed of grains separated by grain boundaries. Grain boundaries are more resistive as compared to grains due to disordered atomic arrangement near the grain boundaries which enhances electron scattering resulting in increased resistivity. It is reported that the electrical properties of ferrites are controlled mainly by grain boundaries [33]. It is well known that larger the crystallite size, lesser the number of grain boundaries and
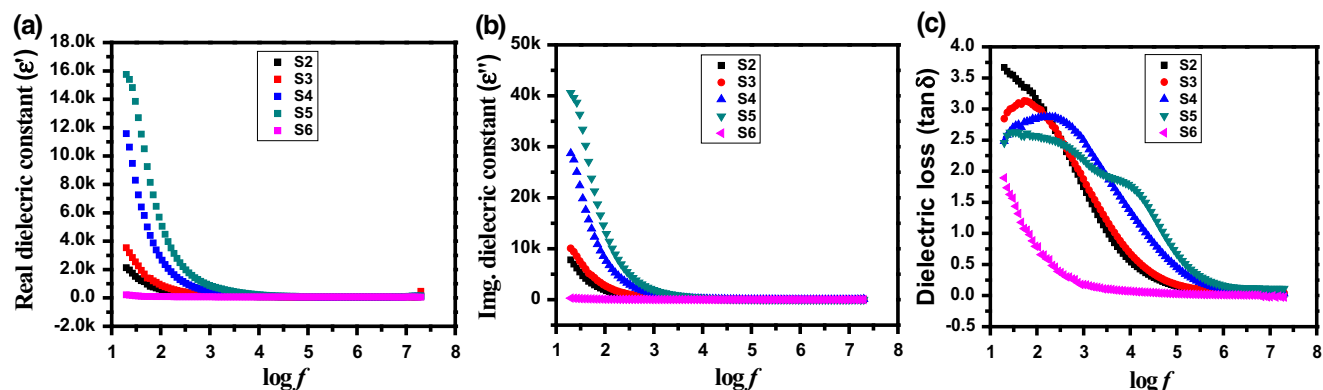

Fig. 3 Frequency dependence of ε′, ε″, and tan δ of BSFMO samples

Fig. 4 a Log σ_{ac} versus log ω for (S2–S6) samples, **b** exponent n as a function of Mn contents
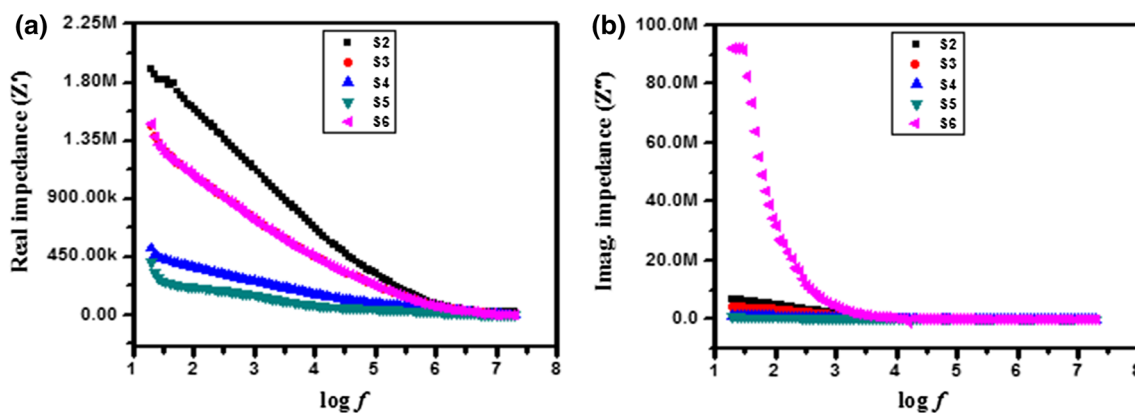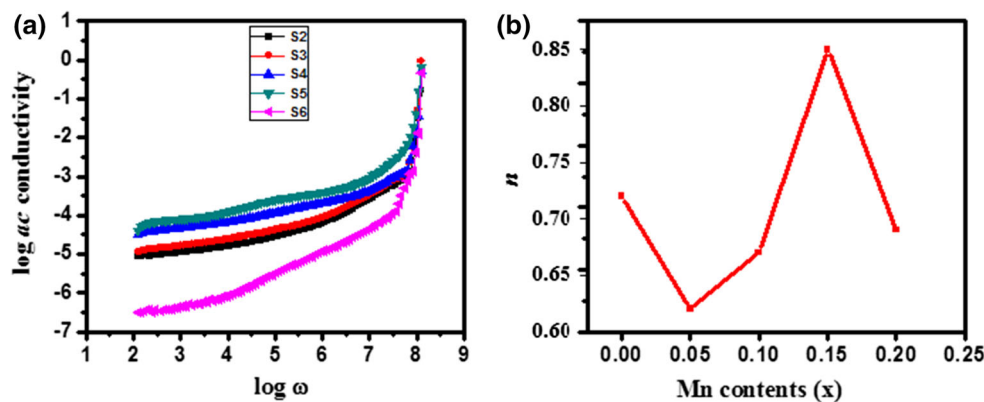

Fig. 5 Frequency dependence of real (Z′) and imaginary (Z″) parts of impedance

vice versa. From Table 1, it can be seen that crystallite size increases with Mn contents due to which number of resistive grain boundaries become lesser resulting in increased conductivity. At higher frequencies, Z′ for all samples coincide with each other, so release of space charge and decrease of barrier properties inside the materials are expected [34].

The dielectric modulus formalism is used to study the dynamical features related to electrical transport within the materials. One advantage of this technique is the suppression of electrode effect. From Fig. 6a, we observe for all samples that in low frequency region, real part of modulus (M′) tends to be very small (approaches to zero) which confirms that contribution of electrode effect is negligible. A continuous dispersion as a function of increasing frequency may be due to conduction phenomenon because of short range mobility of charge carriers. With increasing frequency, M′ reaches a maximum value for all samples (except S2, for which M′ remains almost constant throughout the frequency range). This demonstrates that relaxation processes are spread over an extensive range of frequencies. For S2, Mn = 0, which confirms that M′ remains constant due to the effect of Sr^{2+} while dispersions

in other samples are the result of Mn^{4+} doping in BFO. Figure 6b shows that M″$_{max}$ shifts towards higher frequency side with increase of Mn contents (up to x = 0.15) and frequency. On both sides of M″$_{max}$ peaks are wider and asymmetric which indicate the spread of relaxation times instead of a single time constant, so a non-Debye type relaxation exists [34–36]. For sample S6, M″$_{max}$ moves towards low frequency region, an indication of increased conduction mechanism. Charge carriers are able to move over long and short distances at lower and higher frequencies, respectively. M″$_{max}$ is a symbol of transition from long range to short range mobility. The condition for observing M″$_{max}$ of a material is: $\omega\tau = 1$, here $\omega = 2\pi f_{max}$ and τ is the relaxation time [33].

Nyquist or Cole–Cole plots provide information about the electrical processes occurring inside the materials in the form of semicircular arcs [26] as shown in Fig. 7. The data can be represented in the form of an equivalent electrical circuit with parallel combination of resistance and capacitance as shown in Fig. 8. For sample S2, two semicircular arcs can be observed which indicate two different types of contributions. The high and low frequency semicircles represent the contribution of grains and grain boundaries,
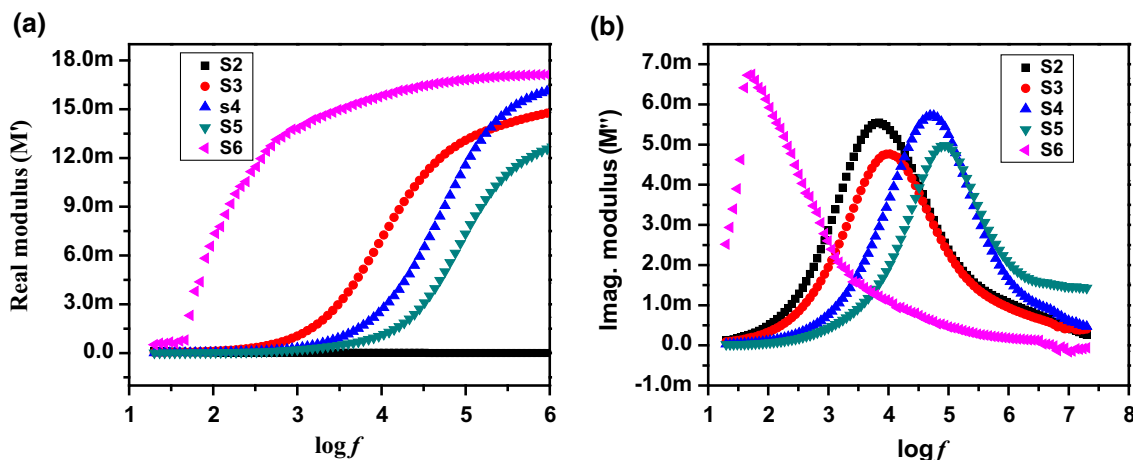
Fig. 6 Frequency dependence of real (M′) and imaginary (M″) parts of electric modulus of BSFMO samples
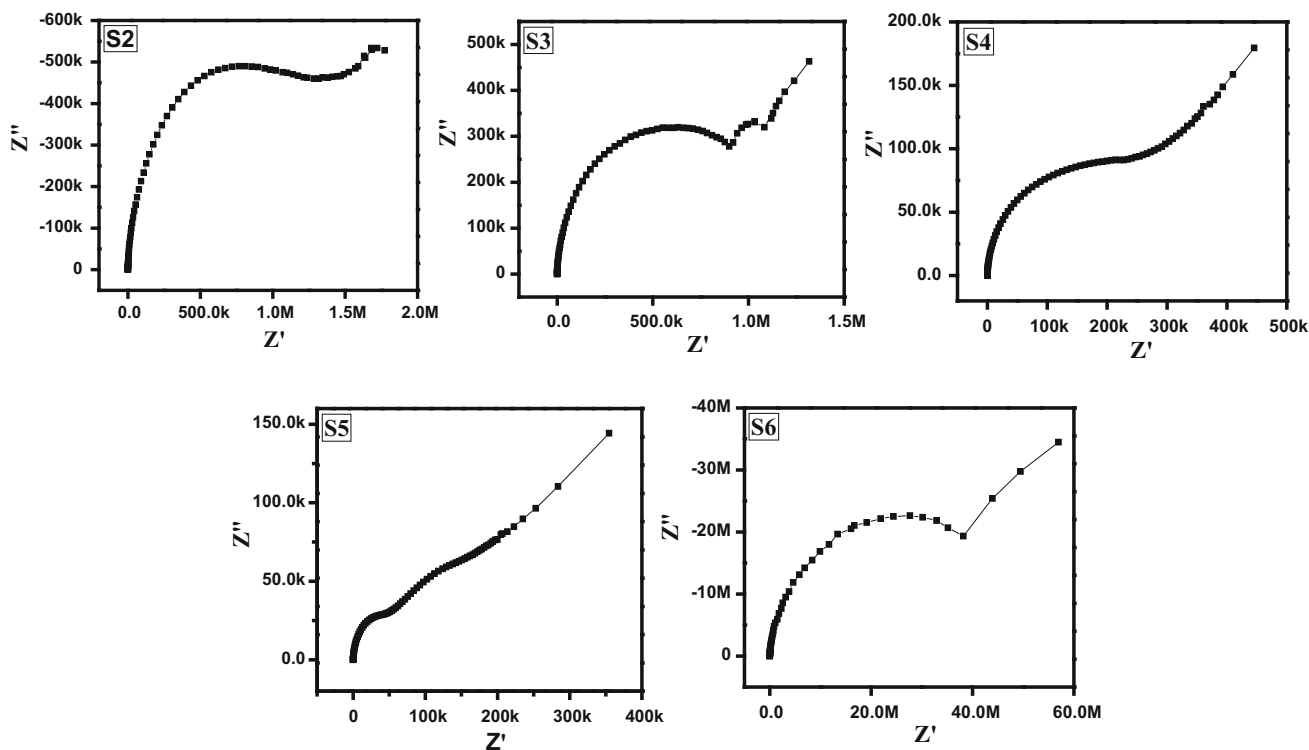

Fig. 7 Cole–Cole or Nyquist plots of samples

respectively. This process can well be explained on the basis of Brick layer model [26]. For sample S3, a third semicircular arc (not a full semicircular arc but somewhat approaches towards the shape) is also observed. This may be attributed to the beginning of polarization effects at the material-electrode interface. The electrode polarization may be neglected because it usually dominates at very low frequencies. Sample S4 displays one semicircular arc and one almost straight line with positive slope, which is the characteristic of very high impedance. For sample S5, two

suppressed, distorted semicircular arcs and one straight line-like that of sample S3 can be seen. Variation in grain size distribution, defects, imperfections, grain boundary stress/strain and volume fraction of the components may be the factors contributing to such behavior [37]. The plot for sample S6, displays one semicircle and one straight line just like that of sample S4 representing the grain and grain boundary effects, respectively. A perfect semi-circle having center at real Z-axis is the characteristic for an ideal Debye-type relaxation. For present study, the distorted
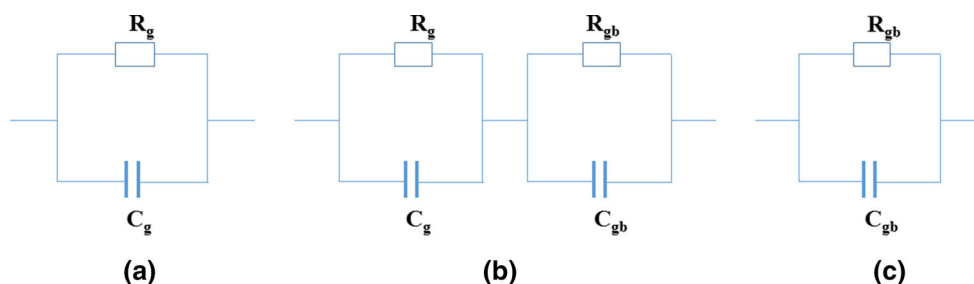
Fig. 8 Equivalent circuits used to represent the electrical properties **a** grain effects, **b** grain and grain boundary effects, and **c** grain boundary effects

Table 3 Grain and grain boundary contribution of the doped compositions

Composition	R_g (MΩ)	C_g (pF)	R_{gb} (MΩ)	C_{gb} (pF)
$Sr_{0.1}Bi_{0.9}FeO_3$	1.4607	1.6804	–	–
$Sr_{0.1}Bi_{0.9}Fe_{0.95}Mn_{0.05}O_3$	1.117	79.2319	1.3	971.3557
$Sr_{0.1}Bi_{0.9}Fe_{0.90}Mn_{0.10}O_3$	0.401	194.1464	–	–
$Sr_{0.1}Bi_{0.9}Fe_{0.85}Mn_{0.15}O_3$	0.7352	14.1150	0.2683	684.8196
$Sr_{0.1}Bi_{0.9}Fe_{0.80}Mn_{0.20}O_3$	52.8635	7.9760	–	–

semicircles, having centers below Z′-axis demonstrate non-Debye type of relaxation. We can calculate capacitance using resistance and f_{max} for each semicircle by following Eq. 4.

$$\omega\tau = 2\pi f_{max} RC = 1 \qquad (4)$$

The calculated values of R_g, C_g, R_{gb} and C_{gb} are listed in Table 3. The high value of R_{gb} is the result of electron scattering due to disordered atomic arrangement at the grain boundaries [31].

4 Conclusion

Polycrystalline NPs of as-burnt $Bi_{0.9}Sr_{0.1}FeO_3$ and $Bi_{0.9}Sr_{0.1}Fe_{1-x}Mn_xO_3$ (x = 0, 0.05, 0.10, 0.15 and 0.20) are prepared successfully using sol–gel auto-combustion method at relatively low temperature. It is concluded that sintering temperature is the most important parameter for developing the crystal phase during the synthesis process of ceramics. A heat treatment at 550 °C, minimum for 3 h, is required to transform the gel into oxide in case of BFO. Sr/Mn doping in BFO has not changed the crystal symmetry of the parent compound. The calculated crystallite sizes are in the range of 9–15 nm while average estimated grain sizes are in the range of 50–80 nm. At higher frequencies, BSFMO NPs exhibit $\varepsilon' > 200$ while $\tan\delta < 1$ which suggests that the present compositions can be used to design microwave/high frequency devices. Non-Debye type relaxation is confirmed from complex impedance spectroscopy. Frequency dependent analysis indicates that there exist an overall correlation between Sr/Mn contents

incorporated, properties and microstructures of BSFMO ceramics. Dielectric and impedance properties are improved with Sr/Mn co-doping in bismuth ferrite.

References

1. S.J. Pearton, W.H. Heo, M.I. Vill, D.P. Norton, T. Steiner, Semicond. Sci. Technol. **19**, 59–74 (2004)
2. H. Schmid, Ferroelectrics **162**, 317–338 (1994)
3. G. Ali, S.A. Siddiqi, S.M. Ramay, S. Atiq, M. Saleem, Int. J. Min. Met. Mater. **20**, 166–171 (2013)
4. S. Mohanty, A. Kumar, R.N.P. Choudhary, J. Mater. Sci. Mater. Electron. **26**, 9640–9648 (2015)
5. G. Catalan, J.F. Scott, Adv. Mater. **21**, 2463–2485 (2009)
6. S. Kumar, J. Mater. Sci. Mater. Electron. **24**, 2112–2115 (2013)
7. G.S. Arya, N.S. Negi, Phys. D: Appl. Phys. **46**, 095004 (2013)
8. V.R. Reddy, D. Kothari, S.K. Upadhyay, A. Gupta, N. Chauhan, A.M. Awasthi, Ceram. Int. **40**, 4247–4250 (2014)
9. M. Singh, Y. Yang, C.G. Takoudis, A. Tatarenko, G. Srinivasan, P. Kharel, G. Lawes, Electrochem. Solid State Electrochem. Solid State **12**, H161 (2009)
10. J.C. Yang, Q. He, P. Yu, Y.H. Chu, Annu. Rev. Mater. Res. **45**, 249 (2015)
11. D. Varshney, A. Kumar, K. Verma, J. Alloys Compd. **509**, 8421–8426 (2011)
12. J. Li, K. Liu, J. Xu, L. Wang, L. Bian, F. Xu, J. Mater. Sci. Res. **2**, 75–81 (2013)
13. J. Wei, D. Xue, Electrochem. Solid-State Lett. **10**, G85–G88 (2007)
14. T. Kawae, H. Tsuda, H. Naganuma, S. Yamada, M. Kumeda, S. Okamura, A. Morimoto, Jpn. J. Appl. Phys. **47**, 7586 (2008)
15. A.K. Ghosh, H. Kevin, B. Chatterjee, G.D. Dwivedi, A. Barman, H.D. Yang, S. Chatterjee, Solid State Commun. **152**, 557–560 (2012)

16. S. Kumari, N. Ortega, A. Kumar, S.P. Pavunny, J.W. Hubbard, C. Rinaldi, G. Srinivasan, J.F. Scott, R.S. Katiyar, J. Appl. Phys. **117**, 114102 (2015)
17. X. Zhang, Y. Sui, X. Wang, J. Tang, W. Su, J. Appl. Phys. **105**, 07D918 (2009)
18. A. Khalid, S. Atiq, S.M. Ramay, A. Mahmood, G.M. Mustafa, S. Riaz, S. Naseem, J. Mater. Sci. Mater. Electron. (2016). doi:10. 1007/s10854-016-4927-1
19. K.S. Nalwa, A. Garg, J. Appl. Phys. **103**, 044101 (2008)
20. S.N. Tripathy, B.G. Mishra, M.M. Shirolkar, S. Sen, S.R. Das, D.B. Janes, D.K. Pradhan, Mater. Chem. Phys. **14**, 423–431 (2013)
21. M.M. Kumar, V.R. Palkar, K. Srinivas, Appl. Phys. Lett. **76**, 2764 (2000)
22. S. Riaz, S.M.H. Shah, A. Akbar, S. Atiq, S. Naseem, J. Sol-Gel. Sci. Technol. **74**, 329–339 (2015)
23. T. Hussain, S.A. Siddiqi, S. Atiq, M.S. Awan, Prog. Nat. Sci. **23**, 487–492 (2013)
24. N. Wang, J. Cheng, A. Pyatakov, A.K. Zvezdin, J.F. Li, L.E. Cross, D. Viehland, Phys. Rev. B **72**, 104434 (2005)
25. C.G. Koops, Phys. Rev. **83**, 121 (1951)
26. J. Rout, R.N.P. Choudhary, H.B. Sharma, S.R. Shannigrahi, Ceram. Int. **41**, 9078 (2015)
27. Y.H. Lee, J.M. Wu, Y.L. Chueh, L.J. Chou, Appl. Phys. Lett. **87**, 172901 (2005)
28. W. Chen, W. Zhu, O.K. Ta, X.F. Chen, J. Appl. Phys. **108**, 034101–034118 (2010)
29. A.K. Jonscher, Nature **267**, 673 (1977)
30. S. Pattanayak, A. Priyadarshan, R. Subudhi, R.K. Nayak, R. Padhee, J. Adv. Ceram. **2**, 235–241 (2013)
31. K.M. Batoo, F.A. Mir, M.S.A. El-sadek, M. Shahabuddin, N. Ahmed, J. Nanopart. Res. **15**, 2067 (2013)
32. H. Singh, A. Kumar, K.L. Yadav, Mater. Sci. Eng. B **176**, 540 (2011)
33. S. Pattanayak, B.N. Parida, P.R. Das, R.N.P. Chaoudhary, Appl. Phys. A **112**, 387–395 (2013)
34. A.K. Behera, N.K. Mohanty, S.K. Satpathy, B. Behera, P. Nayak, Acta. Metall. Sin. Engl. Lett. **28**, 847–857 (2015)
35. P.B. Macedo, C.T. Moynihan, R. Bose, Phys. Chem. Glasses **13**, 171 (1972)
36. Z. Anwar, M.A. Khan, I. Ali, M. Asghar, M. Sher, I. Shakir, M. Sarfraz, M.F. Warsi, J. Ovonic Res. **10**, 265–273 (2014)
37. MdT Rahman, C.V. Ramana, J. Appl. Phys. **116**, 164108 (2014)